Random-access scanning microscopy for 3D imaging in awake behaving animals

K. M. Naga Srinivas Nadella, Hana Roš, Chiara Baragli, Victoria A. Griffiths, George Konstantinou, Theo Koimtzis, Geoffrey J. Evans, Paul A. Kirkby and R. Angus Silver*

Department of Neuroscience, Physiology and Pharmacology, University College London, Gower Street, London, WC1E 6BT, United Kingdom.

Correspondence: a.silver@ucl.ac.uk

Key words

Calcium imaging, two-photon, acousto-optic lens, random-access, synapse, neuron, network, circuit.

Abstract

Understanding how neural circuits process information requires rapid measurements from identified neurons distributed in 3D space. Here we describe an acousto-optic lens two-photon microscope that performs high-speed focussing and line-scanning within a volume spanning hundreds of micrometres. We demonstrate its random access functionality by selectively imaging cerebellar interneurons sparsely distributed in 3D and by simultaneously recording from the soma, proximal and distal dendrites of neocortical pyramidal cells in behaving mice.

Main

Understanding information processing in the brain requires the measurement of signals as they rapidly flow through neuronal circuits, deep within scattering tissue. However, circuits are often arranged in layers, neuronal subtypes are sparsely distributed, and dendrites and axons radiate and branch in 3D space. Since neuronal compartments of interest often occupy a small fraction of total tissue volume, considerably higher temporal resolution could be achieved if regions of interest (ROIs) were selectively imaged rather than the whole volume. Although conventional resonant galvanometer two-photon laser scanners can image rapidly[1] and achieve fast focussing with electrically tuneable[2] or ultrasound lenses[3] or with a pair of matched objective lenses and a small mirror[4], their inertia limits the speed at which they can jump between ROIs. This makes it difficult to monitor sparsely distributed neuronal activity in 3D with conventional imaging methods.

Acousto-optic lens (AOL) microscopes[5-7] can perform inertia-free focussing enabling acquisition of 3D Random-Access Multi-Photon (3D-RAMP) point measurements within an imaging volume at 35-50 kHz[7-10]. However, the major technical limitation of acousto-optic-deflector (AOD)-based scanning, including conventional AOLs, is that they cannot perform full-frame continuous line-scanning away from the natural focal plane of the objective[6,11,12] (**Supplementary note 1,2**). This is problematic for *in vivo* imaging because acquiring Z-stacks is slow using 3D-RAMP voxel-by-voxel pointing[7] or mini-scans (consisting of a few voxels)[9] to form each image, due to their low duty cycle compared to continuous line-scans (**Supplementary Fig. 1a**). Furthermore, brain movement compromises 3D-RAMP pointing, because points of interest shift away from the predefined points where the laser is sequentially focussed. To overcome these limitations, we have developed a compact AOL two-photon microscope that can perform 3D Random-Access Pointing and continuous line-Scanning (3D-RAPS) over the entire imaging volume. This enables high-speed volumetric imaging and a range of new random access 3D imaging modes for monitoring sparsely distributed neuronal activity in awake animals (**Fig 1a**).

Three technical developments were required for AOL-based random access line-scanning. Firstly, custom-designed, thin on-axis AOD crystals, coupled with elliptically polarised light, improved uniformity of diffraction efficiency with deflection angle (**Supplementary Fig. 2a**) and AOL light transmission efficiency (from ~15% to ~25%) over our 1st generation design. Secondly, high-speed line-scanning generated with our custom-designed field programmable gate array (FPGA)-based AOL control system (**Fig 1a; Supplementary Fig. 1b; Methods**) was key in enabling more uniform light transmission over larger scan angles when focussing away from the natural focal plane, as predicted by our model of a spherical AOL[13] (**Fig. 1b**). This occurs because fast scanning reduces the time the AOL is required to focus, allowing more acoustic bandwidth for beam deflection (**Supplementary Note 2**). Thirdly, a high bandwidth FPGA-based acquisition system was synchronised with the AOL control system to acquire red and green fluorescence signals during fast line-scans (**Methods**). These developments resulted in a compact AOL 3D two-photon laser scanner with relatively uniform transmission efficiency across the focussing range (**Supplementary Fig. 2b**). As predicted, the focussing range over which full 512 voxel XY scanning could be performed depended on line-scan speed (**Supplementary Fig. 1c**). Since optical aberrations associated with remote focussing and diffractive optics increase with imaging volume size (**Supplementary Fig. 3**)[6], we restricted high resolution imaging to 250x250x250 µm. This volume could be imaged using full-frame constant velocity line-scans (512x512 or 1024x1024 voxels) with a 50 ns/voxel dwell time (i.e. pixel integration time; **Supplementary Fig. 2c; Supplementary Video 1**), which represents a >255-fold increase in voxel acquisition rate compared to the fastest AOL 3D-RAMP pointing and is comparable to 2D resonant galvanometers and 2D AOD scanners (**Supplementary Table 1**).

To test the *in vivo* performance of our AOL microscope we imaged cerebellum and visual cortex in awake head-fixed mice on a cylindrical treadmill[14]. The objective lens was fixed and focussing and line-scanning performed exclusively by the AOL. The spatial resolution of AOL Z-stack imaging was sufficient to resolve fine structures of L2/3 pyramidal

cells expressing the activity-independent protein tdTomato (**Supplementary Video 1**). Spines were resolvable over the full 250 µm focus range and across the XY field-of-view (FOV; **Supplementary Fig. 4**). In the cerebellum, this focussing range enabled imaging across all three layers of the cortex (**Fig. 1c; Supplementary Fig 5a**). For the fastest full-frame line-scan speed (20 kHz) the AOL could image at 39 Hz at 512x512 voxel resolution. Since the AOL can focus to any location within the imaging volume and start the next line-scan within 24.5 µs, full resolution Z-stacks could be acquired rapidly (**Supplementary Video 2**).

To examine neuronal activity in 3D we expressed the genetically encoded calcium indicator GCaMP6f[15] in the cerebellar cortex and performed multi-plane imaging. Superficial and deep molecular layer interneurons are visible in the upper two images (49 µm and 73 µm from pia), while superficial and deep Golgi cells were recorded in upper and lower regions of the granule cell layer (GCL; at 85 µm and 102 µm from pia) in the four 256x256 voxel images recorded near-simultaneously at 19.5 Hz (**Fig. 1d; Supplementary Fig 5b; Supplementary Video 3**). Following *post hoc* movement correction of images (**Methods**), analysis of the fluorescence revealed calcium signals related to locomotion in these inhibitory interneurons (**Fig. 1d**). These results demonstrate that our AOL microscope design can perform high-speed Z-stacks and multi-plane imaging, overcoming major limitations of previous AOL designs and extending methods for imaging neuronal activity across cortical layers[2,16].

Inhibitory interneurons typically occur at a lower density than excitatory neurons and are sparsely distributed in space. This makes monitoring activity with single or multi-plane imaging inefficient, because the probability of a soma falling within the imaging plane is small (**Supplementary Fig. 6a,b**). To address this we implemented random access patch scanning (**Fig 1a**), enabling the user to define imaging patches intersecting each ROI. Such selective ROI imaging allows more sparsely distributed cells to be monitored at high temporal resolution within the imaging volume (**Supplementary Fig. 6a-c**). The smaller

number of voxels per line used for patches than for full line-scans enabled faster imaging (**Supplementary Fig. 1d**) and a wider range of dwell times (**Supplementary Fig. 2c,d**). Random access patch imaging of cerebellar interneurons at 50 Hz (**Supplementary Video 4**) revealed regular, discrete signalling events during both stationary periods and during locomotion (**Supplementary Fig. 7**). In contrast, patch imaging of L2/3 pyramidal cells co-expressing GCaMP6f and tdTomato (**Supplementary Video 5**) revealed sparse activity that was not clearly related to locomotion (**Fig. 2**). Similar results were obtained across a range of dwell times in animals expressing only GCaMP6f (**Supplementary Fig. 8**). By using a montage of patches for *post hoc* movement correction, we ensured spatial information was present even when GCaMP6f fluorescence dropped to low levels in some cells (**Supplementary Video 5**), enabling accurate determination of masks for functional analysis (**Supplementary Fig. 9**). Key advantages of patch scanning over 3D-RAMP point measurements, which can also be performed with our compact AOL design[6,8], are that ROIs can be imaged with a higher duty cycle (**Supplementary Fig. 1a**) and that spatial information within patches allows *post hoc* correction of brain movement, enabling reliable recordings from awake animals.

Understanding how dendritic activity relates to neuronal output requires measurement from dendrites and soma or axon. However, apical dendrites are often orientated axially towards the pia in *in vivo* preparations, making it difficult to rapidly monitor dendritic and somatic activity simultaneously with current imaging technologies. To examine whether AOL-based patch scanning could solve this problem, we selectively imaged the soma, main dendritic trunk and the tuft nexus of a L5 pyramidal cell expressing GCaMP6f and tdTomato in an awake animal (**Fig. 3a**). Despite the 3 ROIs spanning an extended focal range of 297 µm, with the deepest patch over 400 µm from the pia, robust functional signals could be recorded from each location simultaneously at >200 Hz (**Fig. 3b,c**). Random access patch scanning can also be used to build up sub-volumes (**Fig. 1a**). To examine whether this could provide a more complete picture of dendritic activity we imaged three sub-

volumes encompassing the soma, proximal dendrite and distal dendrite of a layer 2/3 pyramidal cell at 27.9 Hz (**Fig. 3d,e**). This revealed [Ca^{2+}] transients in the dendrites and soma with similar activity patterns (**Fig. 3f**). These results demonstrate that sparsely distributed neuronal structures can be selectively imaged with AOL-based random access patch and sub-volume imaging, substantially faster than with whole volume raster scanning.

Our 3D AOL-scanner extends the functionality of current galvanometer and axial scanning-based 3D two-photon imaging technologies[2-4,16,17] (**Supplementary Table 1; Supplementary Note 3**) and overcomes a major limitation of previous AOL designs by providing ultra-fast inertia-free focussing and continuous, constant-velocity XY line-scanning in any focal plane. The compact dimensions (20x20x30 cm) of our AOL design and location on the optical bench, mean that it can be added to custom-built (**Supplementary Fig. 2e**) or commercial two-photon microscopes[8]. Moreover, recent studies indicate that spatial resolution could be further improved with AOL-based wavefront shaping[18,19]. AOL scanning could also be used in conjunction with fast voltage indicators, photolabile compounds and optogenetic transducers for high-speed 3D photostimulation[20]. Our results show that by enabling 3D-RAPS our AOL microscope design can selectively image sparsely distributed populations of inhibitory interneurons without wasting time imaging 'dead space' in-between. Moreover, its ability to monitor dendritic and somatic activity simultaneously, over large depth ranges at high-speed, provides a new tool for studying dendritic integration in awake behaving animals.

Data Availability Statement

Data are available upon request.

Acknowledgements

Funded by the ERC (294667), the UCL impact PhD programme and the Wellcome Trust (095074). RAS is in receipt of a Wellcome Trust Principal Research Fellowship in Basic Biomedical Science (095667; 203048). CB was funded by the Wellcome Trust PhD

programme (097266). We thank D. Farquharson and A. Hogben from the UCL Biosciences mechanical engineering workshop for the design and fabrication of mechanical components and G. Keller for sharing acquisition code. We acknowledge the GENIE Program and the Janelia Research Campus, Howard Hughes Medical Institute for making the GCaMP6 material available; the Mutant Mouse Resource Research Centre (MMRRC) for the C57BL/6 mGluR2-Cre-IRES-eGFP mouse strain. We thank D. Coyle for excellent technical assistance and D. DiGregorio, T. Fernandez-Alfonso, T. Margrie, A. Valera and T. Younts for comments on the manuscript.

Author Contributions

R.A.S. supervised the project; H.R. and C.B. performed *in vivo* experiments; K.M.N.S.N. analysed the data; V.G. G.K. and K.M.N.S.N. developed microscope control and acquisition systems; K.M.N.S.N., T.K., V.G. and G.J.E. wrote the LabVIEW imaging software; G.J.E. and P.A.K. developed the AOL model and performed simulations; P.A.K., K.M.N.S.N. and R.A.S. designed the microscope; R.A.S., K.M.N.S.N. and P.A.K. wrote the manuscript.

Competing financial interests

The authors declare competing financial interests: details accompany the full text HTML version of the paper at http://www.nature.com/naturemethods/. Patents on the AOL technology have been filed (WO/2008/032061, WO/2011/131933).

References

1 Svoboda, K. & Yasuda, R. Principles of two-photon excitation microscopy and its applications to neuroscience. *Neuron* **50**, 823-839, doi:10.1016/j.neuron.2006.05.019 (2006).

2 Grewe, B. F., Voigt, F. F., van 't Hoff, M. & Helmchen, F. Fast two-layer two-photon imaging of neuronal cell populations using an electrically tunable lens. *Biomed Opt Express* **2**, 2035-2046, doi:10.1364/BOE.2.002035 (2011).

3 Kong, L. *et al.* Continuous volumetric imaging via an optical phase-locked ultrasound lens. *Nat Methods* **12**, 759-762, doi:10.1038/nmeth.3476 (2015).

4 Botcherby, E. J. *et al.* Aberration-free three-dimensional multiphoton imaging of neuronal activity at kHz rates. *Proc Natl Acad Sci U S A* **109**, 2919-2924, doi:10.1073/pnas.1111662109 (2012).

5 Kaplan, A., Friedman, N. & Davidson, N. Acousto-optic lens with very fast focus scanning. *Opt Lett* **26**, 1078-1080 (2001).

6 Kirkby, P. A., Srinivas Nadella, K. M. & Silver, R. A. A compact Acousto-Optic Lens for 2D and 3D femtosecond based 2-photon microscopy. *Opt Express* **18**, 13721-13745, doi:10.1364/OE.18.013720 (2010).

7 Reddy, G. D. & Saggau, P. Fast three-dimensional laser scanning scheme using acousto-optic deflectors. *J Biomed Opt* **10**, 064038, doi:10.1117/1.2141504 (2005).

8 Fernandez-Alfonso, T. *et al.* Monitoring synaptic and neuronal activity in 3D with synthetic and genetic indicators using a compact acousto-optic lens two-photon microscope. *J Neurosci Methods* **222**, 69-81, doi:10.1016/j.jneumeth.2013.10.021 (2014).

9 Katona, G. *et al.* Fast two-photon in vivo imaging with three-dimensional random-access scanning in large tissue volumes. *Nat Methods* **9**, 201-208, doi:10.1038/nmeth.1851 (2012).

10 Froudarakis, E. *et al.* Population code in mouse V1 facilitates readout of natural scenes through increased sparseness. *Nat Neurosci* **17**, 851-857, doi:10.1038/nn.3707 (2014).

11 Roorda, R. D., Hohl, T. M., Toledo-Crow, R. & Miesenbock, G. Video-rate nonlinear microscopy of neuronal membrane dynamics with genetically encoded probes. *J Neurophysiol* **92**, 609-621, doi:10.1152/jn.00087.2004 (2004).

12 Chen, X. *et al.* LOTOS-based two-photon calcium imaging of dendritic spines in vivo. *Nat Protoc* **7**, 1818-1829, doi:10.1038/nprot.2012.106 (2012).

13 Evans, G. J., Kirkby, P. A., Naga Srinivas Nadella, K. M., Marin, B. & Angus Silver, R. Development and application of a ray-based model of light propagation through a spherical acousto-optic lens. *Opt Express* **23**, 23493-23510, doi:10.1364/OE.23.023493 (2015).

14 Ozden, I., Dombeck, D. A., Hoogland, T. M., Tank, D. W. & Wang, S. S. Widespread state-dependent shifts in cerebellar activity in locomoting mice. *PLoS One* **7**, e42650, doi:10.1371/journal.pone.0042650 (2012).

15 Chen, T. W. *et al.* Ultrasensitive fluorescent proteins for imaging neuronal activity. *Nature* **499**, 295-300, doi:10.1038/nature12354 (2013).

16 Yang, W., Miller, K., Carrillo-Reid, L., Pnevmatikakis, E., Paninski, L., Yuste, R., Peterka, D.S.,. Simultaneous multi-plane imaging of neural circuits. *Neuron* **89**, 269-284 (2016).

17 Cheng, A., Goncalves, J. T., Golshani, P., Arisaka, K. & Portera-Cailliau, C. Simultaneous two-photon calcium imaging at different depths with spatiotemporal multiplexing. *Nat Methods* **8**, 139-142, doi:10.1038/nmeth.1552 (2011).

18 Akemann, W. *et al.* Fast spatial beam shaping by acousto-optic diffraction for 3D non-linear microscopy. *Opt Express* **23**, 28191-28205, doi:10.1364/OE.23.028191 (2015).

19 Konstantinou, G. *et al.* Dynamic wavefront shaping with an acousto-optic lens for laser scanning microscopy. *Optics Express* **24**, 6283-6299, doi:10.1364/OE.24.006283 (2016).

20 Emiliani, V., Cohen, A. E., Deisseroth, K. & Hausser, M. All-Optical Interrogation of Neural Circuits. *J Neurosci* **35**, 13917-13926, doi:10.1523/JNEUROSCI.2916-15.2015 (2015).

Figure legends

Figure 1. Acousto-optic lens (AOL) two-photon microscope and random access multi-plane imaging across layers of the cerebellar cortex of an awake mouse. **a**) Schematic diagram of the AOL 3D random access two-photon microscope configured for *in vivo* imaging. Inset box: Schematic diagram showing full Z-stack, multi-plane, sub-volume and patch scanning modes together with pointing. Imaging speed calculated for line-scanning and pointing mode using 50 ns and 4 µs dwell time, respectively. **b**) Theoretical relationship between AOL transmission efficiency and scan angle for different voxel dwell times when the AOL is focussed to 1 m (equivalent to Z=+135 µm with a 20x objective). **c**) AOL Z-stack (136 planes with 2 µm step at 100 ns dwell time) of GFP expressing inhibitory interneurons in mouse cerebellum. **d**) Averaged images of cerebellar interneurons expressing GCaMP6f in 4 planes acquired near-simultaneously at 19.5 Hz (100 ns/voxel), after *post hoc* movement correction. Coloured squares indicating the neuronal structures from which the fluorescent traces (right) were extracted. Background colours indicate layers in **Supplementary Fig 5a**. Grey trace at the bottom shows the speed of animal, with grey shading indicating periods of locomotion. Vertical bar indicates normalized change in fluorescence (ΔF/F) together with speed of locomotion (cm/s); and the horizontal scale bar indicates time (s).

Figure 2. Random-access patch imaging of neurons in layer 2/3 of primary visual cortex in an awake behaving mouse. **a**) Maximum intensity projection of red channel for cells in layer 2/3 of visual cortex sparsely expressing td-Tomato and GCaMP6f. **b**) Location of 14 X-Y patches within the imaging volume, distributed between 74 µm to 163 µm below the pia. **c**) Averaged images of cellular structures (green channel) scanned near-simultaneously at 50 ns/voxel in the 14 patches (51 x 50 voxels, 22 µm x 21.5 µm) after *post hoc* correction for brain movement. Traces to the right show ΔF/F responses extracted from each patch (52.8 Hz patch cycle rate, i.e. 1/(time to scan all patches)). Grey trace at the bottom shows the speed of the animal on the cylindrical treadmill. Blue-grey shading indicates periods of locomotion. Scale bars as defined in figure 1 legend.

Figure 3. Simultaneous dendritic and somatic imaging of pyramidal neurons in the visual cortex of awake mice. **a**) Partially reconstructed image of a layer 5 neuron within the imaging volume (red box) together with the location of 3 user-selected patches intersecting the soma, apical dendrite and the nexus of the distal dendritic tuft. **b**) Averaged images of the soma and dendritic structures scanned near-simultaneously at 100 ns/voxel in the 3 patches (67 x 51 voxels, ~31 µm x ~23 µm) after *post hoc* correction for brain movement, together with mask outlines (green lines) for extraction of functional data. The acquisition rate was 209 Hz for the 3 patch cycle. Traces to the right show ∆F/F responses extracted from each colour coded patch while the animal was stationary. Dashed black box indicates measurements from the soma and dendrites that were confirmed to be from the same reconstructed cell, while the two other dendrites could not be unequivocally confirmed from the Z-stack image. Grey trace at the bottom shows the speed of the animal on the cylindrical treadmill. **c**) As for **b** but during locomotion. **d**) Two planes showing the somatic and dendritic sections of cells in layer 2/3 visual cortex sparsely expressing td-Tomato and GCaMP6f. **e**) Location of 3 sub-volumes within the imaging volume together with a partial reconstruction of an imaged L2/3 neuron that includes the soma, proximal dendrite and distal dendrite. Each sub-volume consists of 5-6 planes (224 x 59 voxels, 96 µm x 25 µm) 4 µm apart. **f**) Images of different regions of the pyramidal cell from the planes making up each sub-volume after *post hoc* movement correction. Traces show ΔF/F responses extracted from the cellular component present in each plane, where red, green and blue indicate soma, proximal dendrite and distal dendrite, respectively. Data were acquired at 50 ns/voxel with a sampling rate of 27.9 Hz for the 3 volume cycle. Grey trace at the bottom shows the speed of locomotion of the animal on the cylindrical wheel. Blue-grey shading indicates periods of locomotion. Scale bars as defined in figure 1 legend.

ONLINE METHODS

Compact Acousto-Optic Lens 3D two-photon microscope

The optical layout of the 3D Acousto-Optic Lens (AOL) two-photon microscope (**Fig. 1a**) consisted of a Femtosecond laser (2 W at 920 nm; Chameleon Ultra II, Coherent Inc.), a custom designed prism-based pre-chirper that introduced -29000 fs^2 group velocity dispersion (APE GmbH, Berlin), a Pockels cell (Model 350-80LA, Conoptics) and a beam expander that filled the 15 mm aperture of the AOL[6]. The second generation compact configuration AOL reported here consists of two orthogonally arranged pairs of on-axis TeO_2 AODs (Gooch and Housego). AODs were interleaved with quarter wave plates and polarizers to couple the beam into subsequent AODs and also to block the unwanted zero order beam. Acoustic transducers on the first AOD of each pair were wider than the second AOD[6] to maximize diffraction efficiency and the input angle range, respectively. The compact AOL assembly was contained in a 20x20x30 cm box located on the optical table and coupled to a custom-built microscope via a 4f relay (**Supplementary Fig. 2e**). Compact AOLs can also be added to commercially available two-photon microscopes with a pre-chirper by centring the position of the galvanometer mirrors[8].

The microscope consisted of an in-house optical arrangement mounted on top of a SliceScope (Scientifica, UK) with a tube lens, arranged to under-fill a water immersion objective (Olympus XLUMPlanFLN 20X, NA1.0), with an excitation numerical aperture of 0.6 - 0.7, giving a spatial resolution as quantified in **Supplementary Fig. 3**. The two-channel detection system consisted of a dichroic mirror (575dcxr, Chroma Inc.) and emission filters (HQ 525/70m-2P and HQ 630/100m-2P). Green light was detected with GaAsP PMT (H7422, Hamamatsu, Japan) and red light with either a standard PMT (R9880U-20, Hamamatsu, Japan) or a GaAsP (H7422, Hamamatsu, Japan). Output signals from the PMTs were amplified using 200 MHz pre-amplifiers (Series DHPVA 100/200 MHz, FEMTO). The mechanical focus and stage were both motorised (Scientifica Model-MMBP) and

computer controlled. The animals were head fixed using two custom built retractable arms that mounted onto the animal head plate. The treadmill consisted of a Styrofoam cylinder and locomotion was detected with a rotary encoder (RI58, Hengstler, Germany).

The custom designed FPGA AOL control system (**Supplementary Fig. 1b**) consisted of a Xilinx ML506 card and a Texas Instruments DAC card (DAC5672EVM)[19]. Commands to control the loading and execution of the frequency records for 3D AOL random-access raster scanning, patch imaging, multi-volume and pointing were generated by the PC and encoded as RAW Ethernet packets, before being transmitted to the AOL controller via a Gigabit Ethernet interface. The AOL control FPGA used an on-chip, direct digital synthesiser to generate the specified acoustic frequency chirps and these were executed upon receiving a start trigger from data acquisition system. The synthesised digital waveforms were converted into analogue signals by Digital-to-Analog Converters (Texas Instruments, DAC5672EVM) and amplified by 4 RF amplifiers before being fed into the AODs. The FPGA AOL control system design and compiled firmware are available for non-commercial research on request.

The acquisition system consisted of a high speed ADC (800 MHz, dual channel, NI-5772) together with an FPGA (NI FlexRIO – 7966R) that enabled forty-fold oversampling for dwell times of 50 ns. The DAQ FPGA acted as the master, synchronising the AOL acoustic frequency ramps and the data acquisition, allowing dwell times of 50–500 ns for scanning and 50-8000 ns for pointing. Signals were down sampled on the DAQ FPGA by integrating over each voxel dwell time before sending frames to the host PC via the National Instruments PXIe interface. Voxel integration was not synchronised to the 80 MHz laser pluses. Peripherals were controlled using a PXI 6733 card.

The data acquisition software running on the NI FPGA and the user interface (UI) running on Windows PC were developed in LabVIEW and information was exchanged via NI PXIe interface. The software architecture is modular and can instruct the AOL-control system to perform a number of imaging modes including continuous full frame raster scanning, fast Z-

stacks, random-access sub-volume imaging, random-access patch imaging, 3D RAMP pointing as well as setting the resolution, field of view, zoom and dwell time. In order to compensate for the effects of tissue scattering, excitation intensity was adjusted as a function of depth using a Pockels cell. Powers used for *in vivo* imaging were typically 20 - 60 mW, depending on imaging depth. The size of patches was chosen so that the object of interest remained within the patch. In practice, this does not necessarily lead to a reduction in temporal resolution as the voxel resolution of the patch can be reduced as the size is expanded. Acquired data was continuously streamed to disk and depending on the type of recording stored as TDMS, TIFF, or AVI files.

***In vivo* functional imaging in awake behaving mice.** All procedures were carried out in accordance with institutional animal welfare guidelines and licensed by the UK Home Office. We transfected neurons in the mouse visual cortex and cerebellar cortex with a genetically encoded calcium indicator GCaMP6f[15]. Dual sparse labelling in the visual cortex was achieved by co-injecting Cre recombinase (AAV9.CamKII0.4.Cre.SV40, diluted 1:10,000, UPenn Vector Core) with Flex-GCamp6f (AAV1.Syn.Flex. GCamp6f.WPRE.SV40, diluted 1:2) in Ai9 cre-reporter tdTomato[15] transgenic adult mice (tdTomato mice (B6;129S6-*Gt(ROSA)26Sor*$^{tm9(CAG\text{-}tdTomato)Hze}$/J). The somata of cells expressing tdTomato and GCamp6f appear filled (e.g. **Fig. 2**), due to the spectral overlap between tdTomato and GCaMP6f. In contrast, when GCaMP6f is expressed alone, somata had a hollow appearance (**Supplementary Fig. 8**). For these animals, Cre recombinase (AAV9.CamKII0.4.Cre.SV40, diluted 1:5,000) and Flex-GCamp6f (AAV1.Syn.Flex. GCamp6f.WPRE.SV40, diluted 1:2) were co-injected in C57Bl/6 mice. For the cerebellar imaging, either the GAD65-GFP transgenic mouse strain was used or a mGluR2-Cre-IRES-eGFP mouse strain (B6;FVB-Tg(Grm2-cre,-EGFP)631Lfr/Mmuc). For functional measurements, mice were injected with the virus construct AAV1.SynFlex.GCaMP6f.WPRE.SV40 (UPenn Vector Core) into the cerebellar cortex. Stereotaxic virus injections were performed on mice of both sexes, (three male, two female) between P30-P50 for the experiments on visual cortex and older than P60 for experiments in cerebellum. Animals were anaesthetised with ketamine/xylazine, and were slowly injected with a 10-100 nL of suspended virus at a depth of 100-400 µm. A

cranial window was made by placing a 4 mm coverslip gently over the craniotomy and implanting a head plate onto the skull with dental cement. Mice were familiarised with the setup for 1-3 days and then imaged from 4 weeks after viral injection. Mice were free to stand or run on the cylindrical Styrofoam wheel during imaging.

Data format and analysis: Raw imaging data was stored as TIFF images for each time series of the plane/patch. TIFF images were corrected for brain motion using the sequential image analysis software suite (SIMA)[21]. For patch imaging, movement was either corrected patch-by-patch or using a montage of all the patches. The latter approach was particularly effective for imaging ROIs that were sparsely active and in mice expressing only GCaMP6f (**Supplementary Video 6**). Functional signals were extracted from images by generating masks of cellular structures (**Supplementary Figure 9**) using a thresholding algorithm or the thresholding and particle analysis (ImageJ). The average of the intensity of voxels across the mask was calculated for each frame and ΔF/ F calculated. The timing of each data point was calculated at the centre of the ROI.

ImageJ and neuTube (eneuro.org/content/early/2015/01/02/ENEURO.0049-14.2014) were used for 3D rendering and to adjust brightness and contrast of the images for display purposes. No deconvolution or nonlinear scaling such as gamma correction was used on the data for fluorescence traces.

Software Availability

The SilverLab LabVIEW Imaging Software is available on GitHub: https://github.com/SilverLabUCL/SilverLab-Microscope-Software.

References

21 Kaifosh, P., Zaremba, J. D., Danielson, N. B. & Losonczy, A. SIMA: Python software for analysis of dynamic fluorescence imaging data. *Front Neuroinform* **8**, 80, doi:10.3389/fninf.2014.00080 (2014).

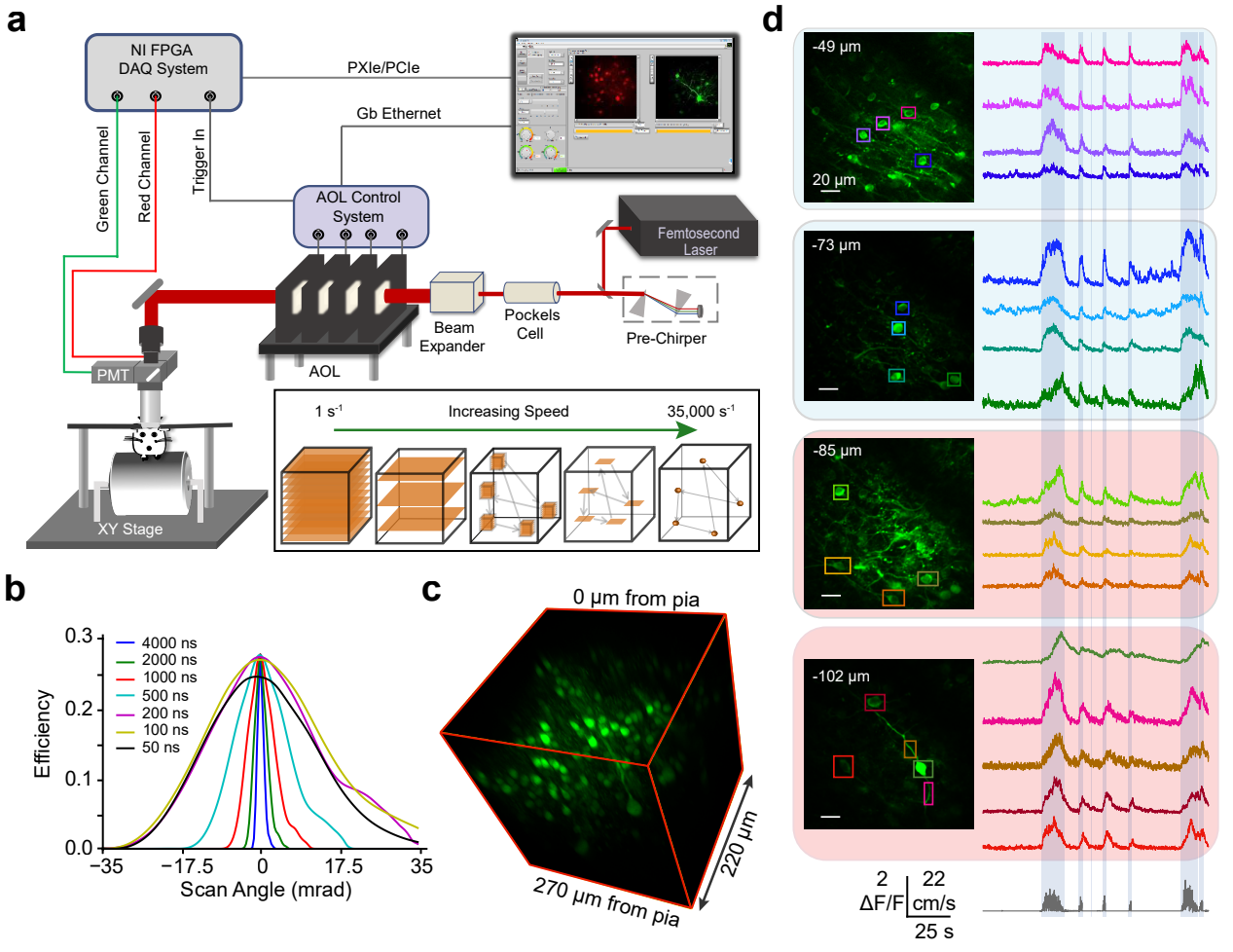
a
NI FPGA
DAQ System
PXIe/PCIe
Gb Ethernet
Green Channel
Red Channel
Trigger In
AOL Control
System
Femtosecond
Laser
Beam
Expander
Pockels
Cell
Pre-Chirper
AOL
PMT
XY Stage
1 s-1
Increasing Speed
35,000 s-1
b
Efficiency
0.3
0.2
0.1
0.0
4000 ns
2000 ns
1000 ns
500 ns
200 ns
100 ns
50 ns
−35
−17.5
0
17.5
35
Scan Angle (mrad)
c
0 µm from pia
220 µm
270 µm from pia
d
-49 µm
20 µm
-73 µm
-85 µm
-102 µm
2
ΔF/F
22
cm/s
25 s

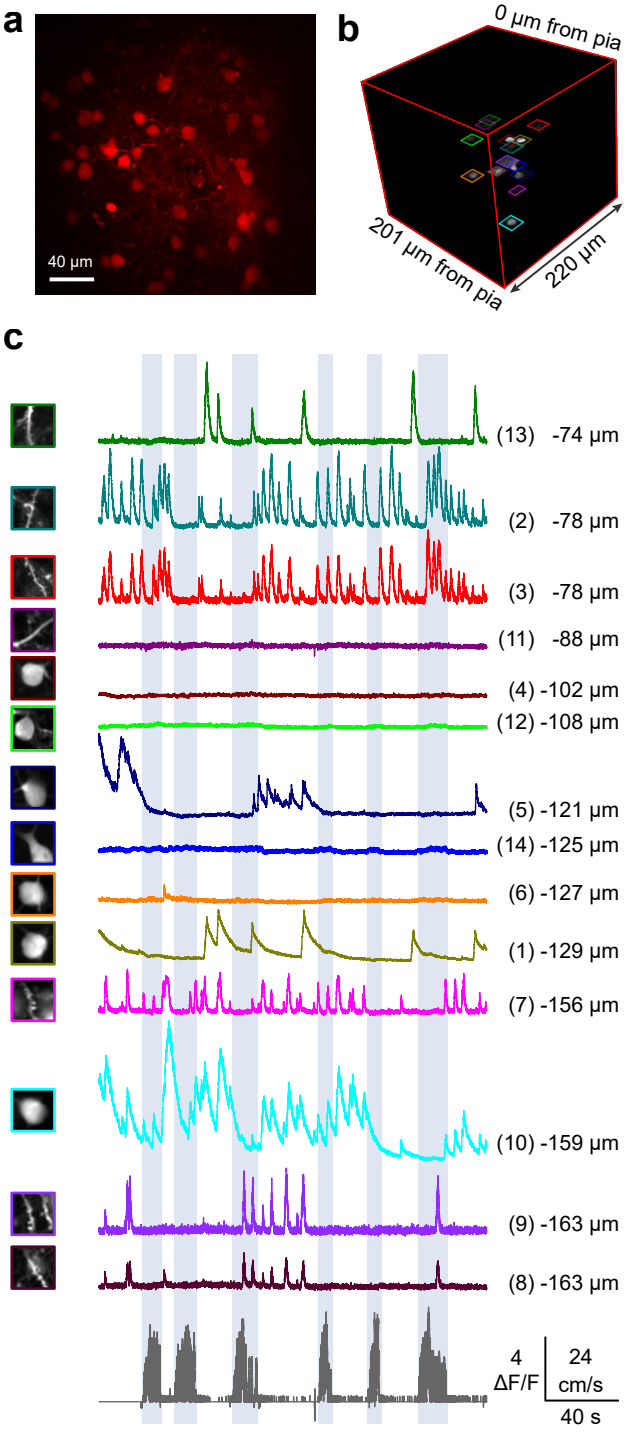
a
40 µm
b
0 µm from pia
201 µm from pia
220 µm
c
(13) -74 µm
(2) -78 µm
(3) -78 µm
(11) -88 µm
(4) -102 µm
(12) -108 µm
(5) -121 µm
(14) -125 µm
(6) -127 µm
(1) -129 µm
(7) -156 µm
(10) -159 µm
(9) -163 µm
(8) -163 µm
4
ΔF/F
24
cm/s
40 s

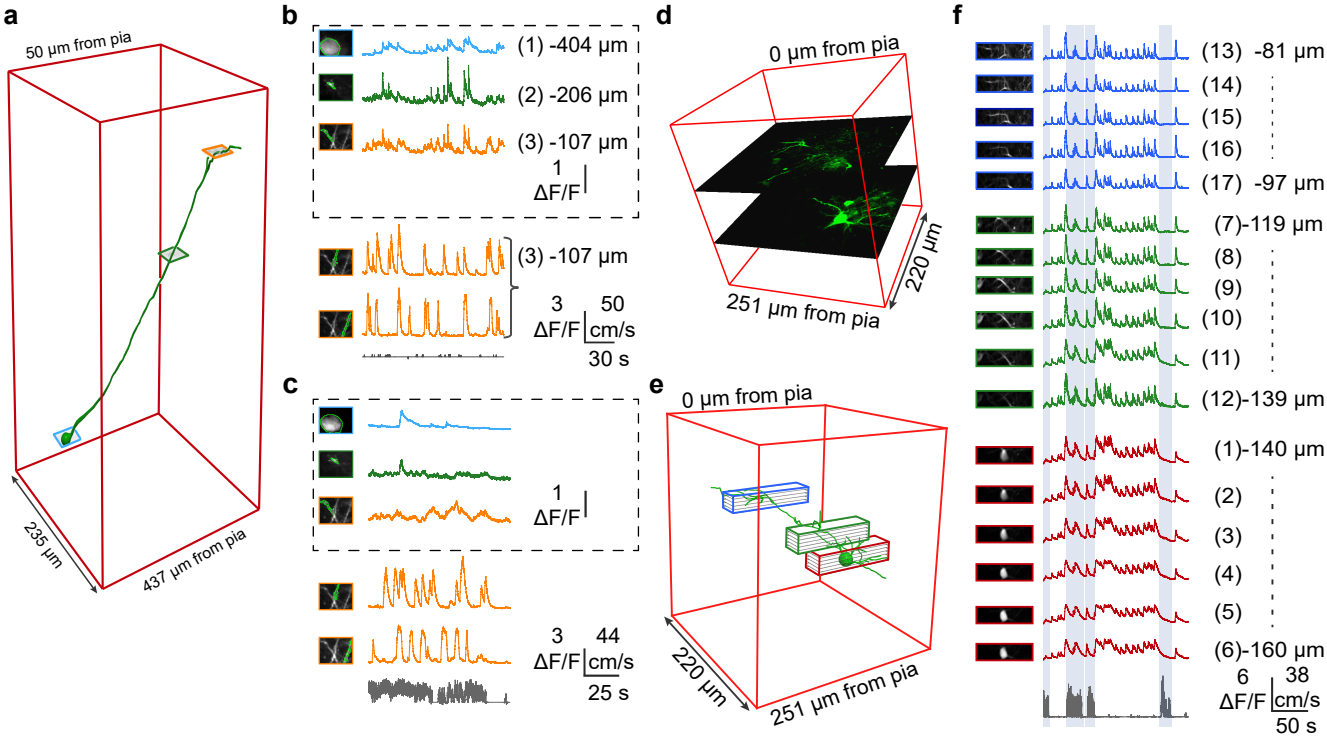
a
50 µm from pia
235 µm
437 µm from pia
b
(1) -404 µm
(2) -206 µm
(3) -107 µm
1
ΔF/F
(3) -107 µm
3
ΔF/F
50
cm/s
30 s
c
1
ΔF/F
3
ΔF/F
44
cm/s
25 s
d
0 µm from pia
220 µm
251 µm from pia
e
0 µm from pia
220 µm
251 µm from pia
f
(13) -81 µm
(14)
(15)
(16)
(17) -97 µm
(7)-119 µm
(8)
(9)
(10)
(11)
(12)-139 µm
(1)-140 µm
(2)
(3)
(4)
(5)
(6)-160 µm
6
ΔF/F
38
cm/s
50 s

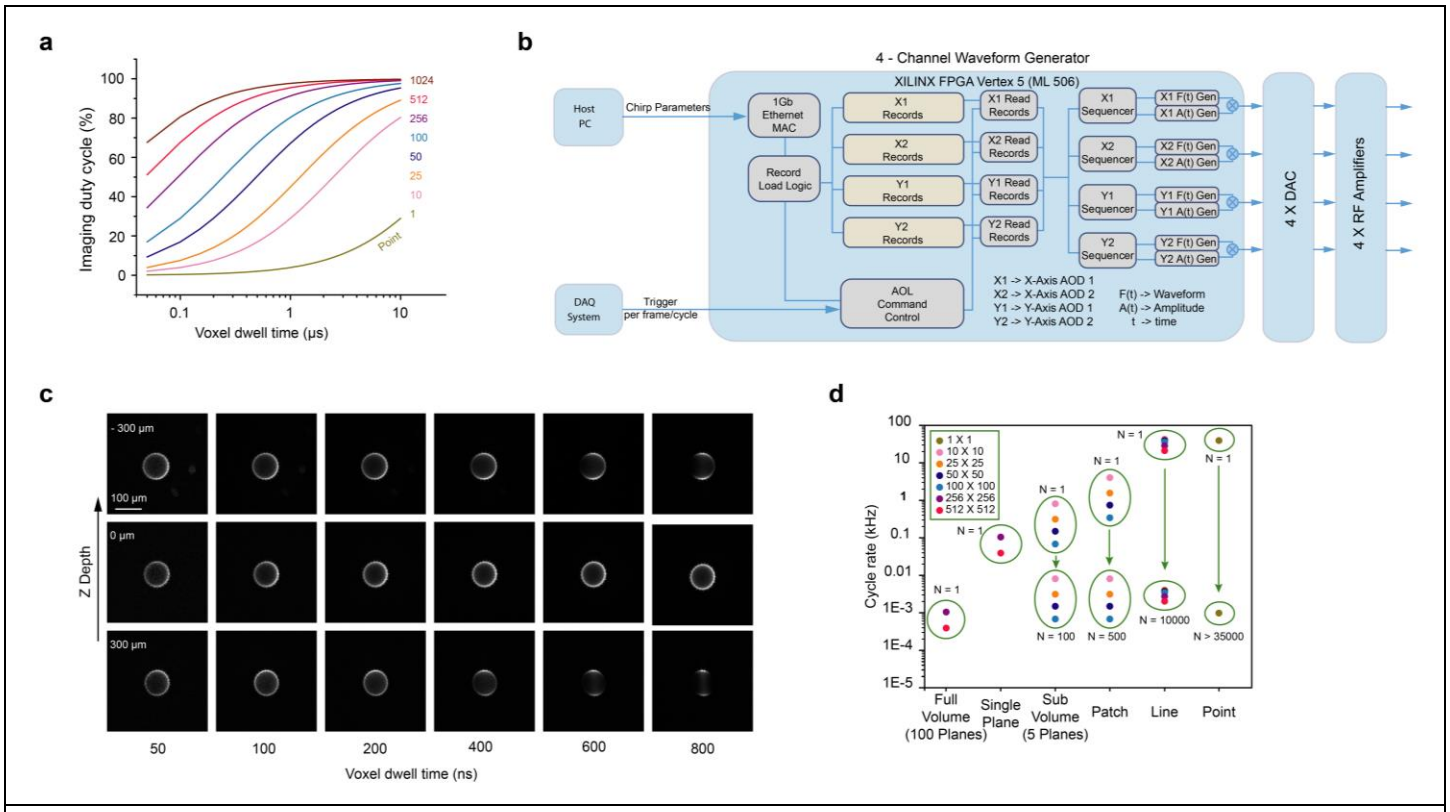

Supplementary Figure 1

Random-access pointing and scanning performance of a 3D acousto-optic lens (AOL) microscope, its FPGA control system and the measured effect of dwell time on imaging volume.

a) Imaging duty cycle as function of voxel dwell time and number of voxels per line-scan assuming 24.5 µs AOL fill-time (where duty cycle = number of voxels x voxel dwell time / (number of voxels x voxel dwell time + AOL fill-time). **b**) Schematic diagram of custom FPGA logic for the AOL control system showing four channels that generate the radio frequency acoustic waves functions (F(t)) and their amplitudes (A(t)). **c**) Pollen grain imaged with AOL line-scanning using a 380 µm field of view at different dwell times. Top row shows imaging at -300 µm focal depth with dwell times from 50 ns to 800 ns. Middle row shows imaging at natural focal plane of the objective (0 µm) and bottom row shows imaging at a Z depth of +300 µm at different dwell times. For dwell times longer than 200 ns a reduction in brightness at the edges of the pollen grain can be observed when focusing 300 µm above or below the natural focal plane due to a fall-off in AOL diffraction efficiency. This effect is not evident for the 50 ns, 100 ns or 200 ns dwell times as predicted from the model (Fig. 1b). **d**) Estimated cycle rates for various imaging modes with AOL scanning and pointing. In the case of single plane and full volumes, 256 x 256 and 512 x 512 are considered. Sub-volume cycle rate was computed assuming 5 planes per sub volume with patch sizes of 10 x 10, 25 x 25, and 50 x 50 voxels. Arrows indicate a range of acquisition rates as the number (N) of planes, sub-volumes, patches and points are increased from 1.

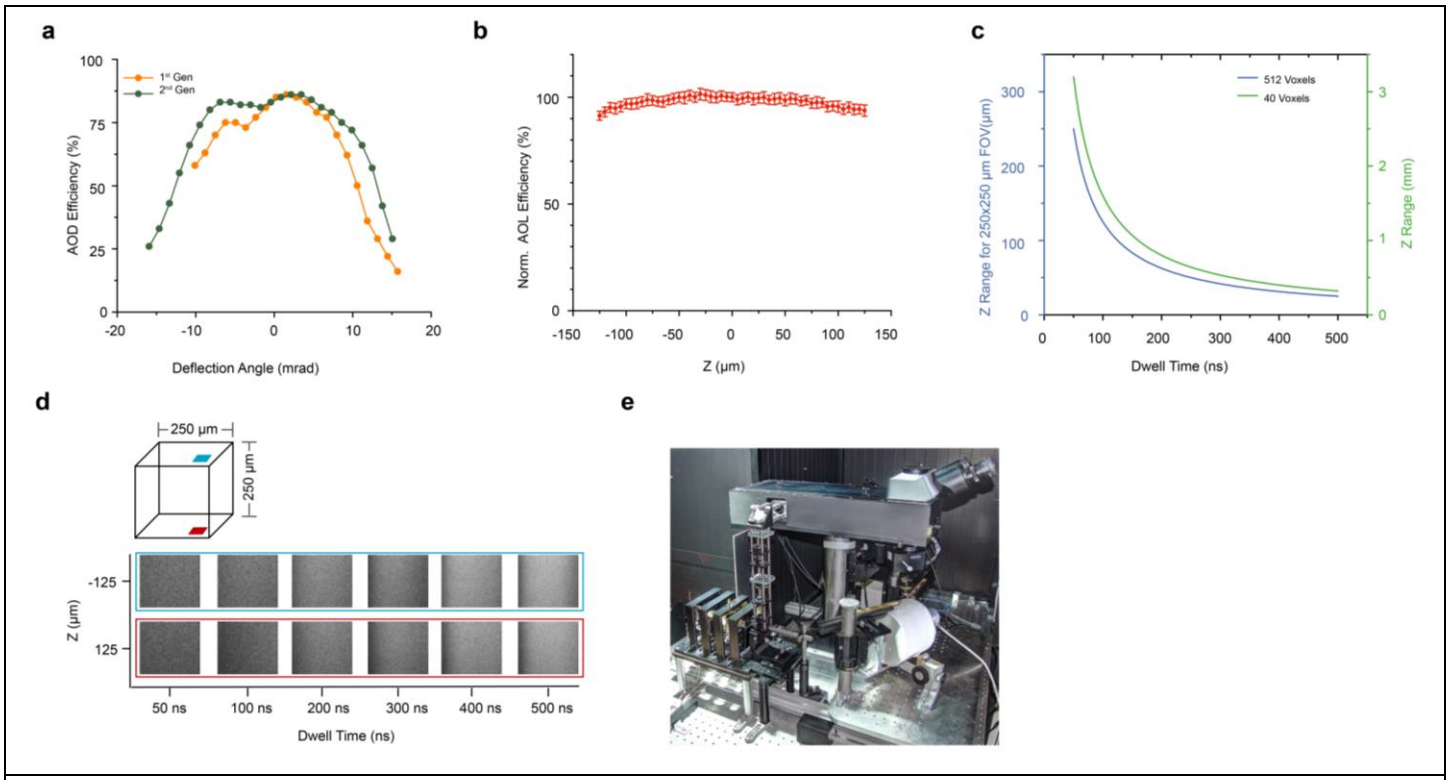

Supplementary Figure 2

Diffraction efficiency of acousto-optic deflectors (AOD) and acousto-optic lens (AOL) and dependence of focusing range on dwell time for full frame and patch imaging.

a) The relationship between diffraction efficiency and AOD deflection angle (centred on the central drive frequency) for 1st generation and 2nd generation crystal design. Measurements were performed at 3W acoustic drive power and at 800 nm optical wavelength. **b**) Light transmission efficiency (normalised to natural focal plane) of second generation AOL measured with a photodiode at 920 nm wavelength over a +/- 125 µm axial range. Error bars indicate standard deviation. **c**) Theoretical relationship between AOL focusing range for full frame (250 µm x 250 µm FOV) 512 voxel line-scans and dwell time (blue line, left axis). Relationship between AOL focusing range and dwell time for 40 x 40 voxel patch (green line, right axis). **d**) Averaged patch images (40 x 35 voxels, 19.5 µm x 17.09 µm) of a fluorescent chroma slide at +/- 125 µm AOL focal planes imaged at 50 ns to 500 ns. Top right schematic shows patch location within the imaging volume, with colour code. **e**) Image of AOL microscope on a 1.5 m x 1.5 m optical table showing AOL assembly and 4f relay into the microscope.

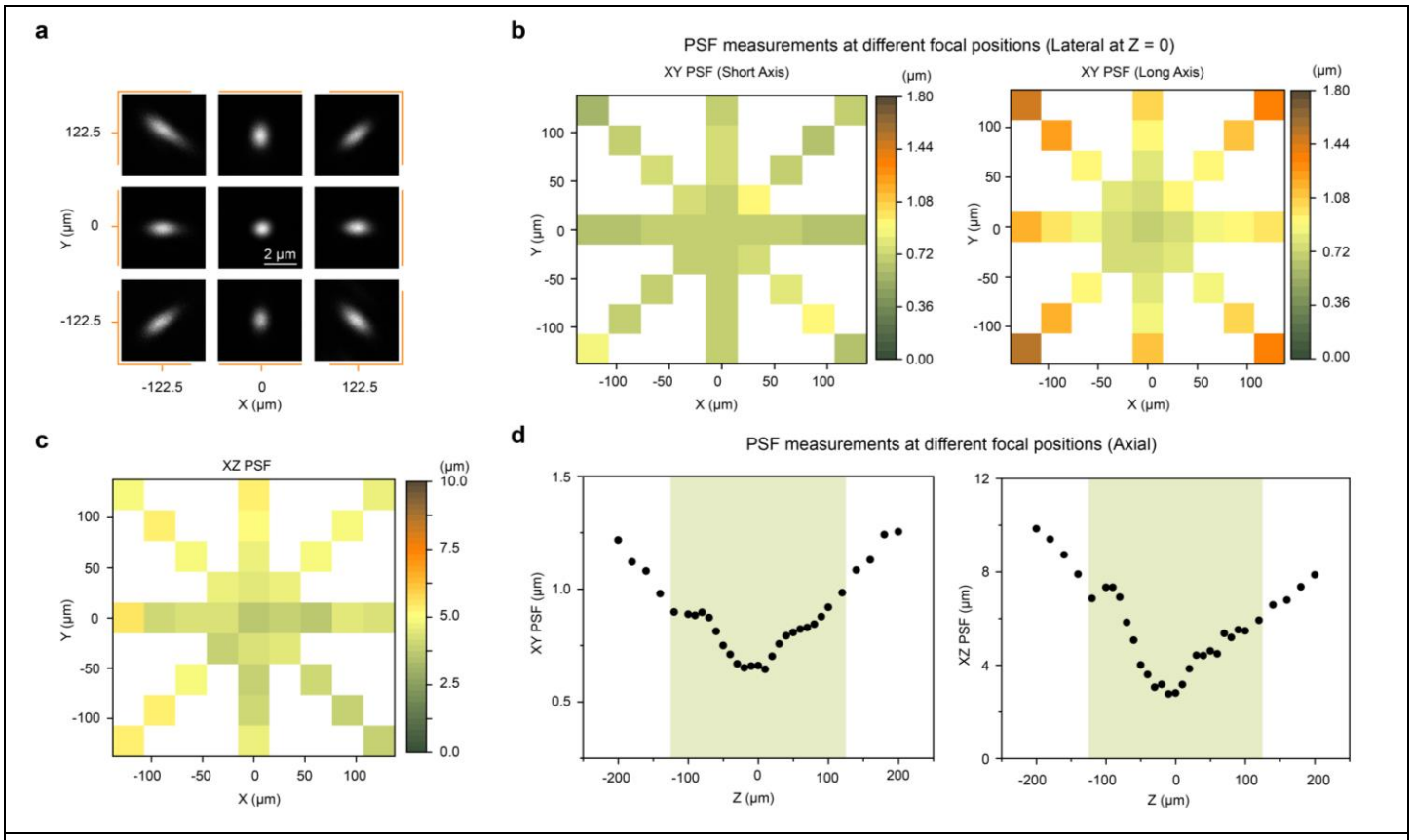

Supplementary Figure 3

Properties of the two-photon point spread function (PSF) across the imaging volume.

a) Montage of images of 200 nm fluorescent beads at the centre (X, Y, Z: 0, 0, 0) of the imaging volume and at the corners of a 245 µm x 245 µm FOV at the natural focal plane. Note the radial elongation of the PSF at the corners. **b**) Left: short axis of PSF measured from 200 nm beads as a function of location across the XY FOV (Z=0). Right: long axis of PSF measured from 200 nm beads as a function of location across the XY FOV (Z=0). At the centre of the natural focal plane the XY resolution is ~0.65 µm and the axial resolution is ~ 3.75 µm. The radial increase in long axis is due to chromatic aberration. **c**) Size of PSF in XZ axis at various lateral positions across the natural focal plane. **d**) Left panel shows XY PSF and right panel shows XZ PSF as a function of distance from the natural focal plane, measured at the centre of each Z plane. Green region indicates the restricted AOL focussing range that we used, where the lateral resolution is <1 µm and the axial resolution of <8 µm. Increases in the PSF away from the natural focal plane are predominantly due to spherical aberration.

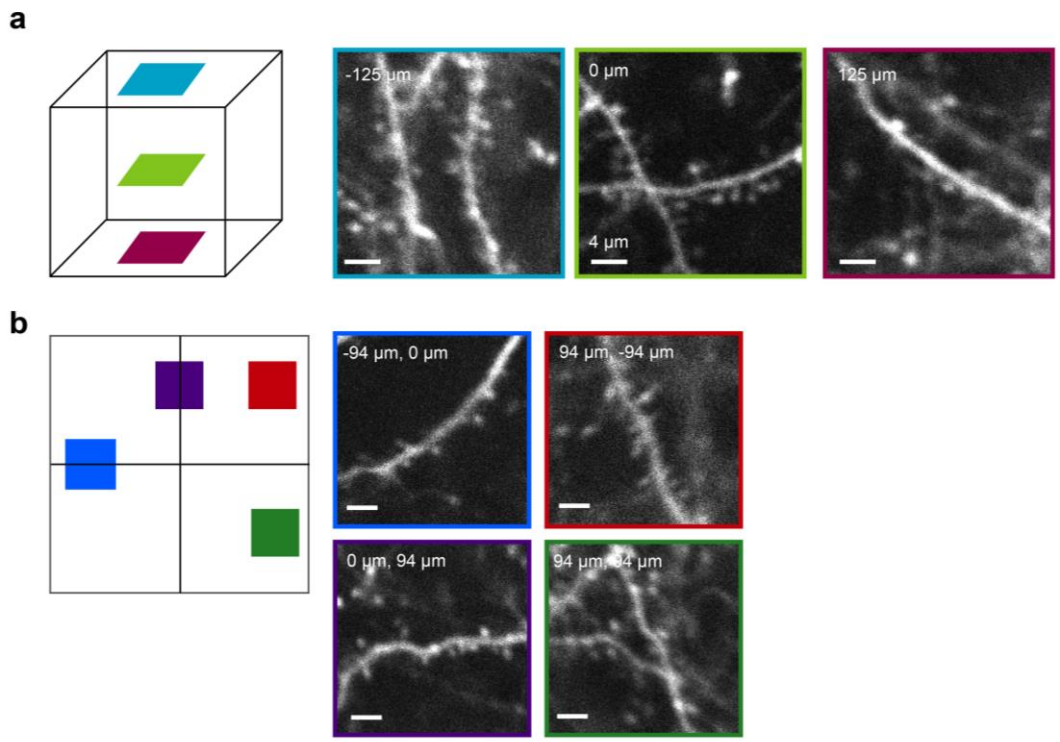

Supplementary Figure 4

Imaging spines and dendrites at various lateral and axial positions within a 250 µm x 250 µm x 250 µm imaging volume in an awake mouse.

a) Left: schematic diagram of imaging volume and colour-coded regions of interest (ROIs) at different focal planes. Fluorescent images of dendrites and spines expressing tdTomato at three different axial positions: -125 µm, 0 µm, and +125 µm, with outlines corresponding to focal plane colour. **b**) Left: schematic diagram of XY field of view at Z=0 with positions of ROIs colour-coded. Fluorescent images of dendrites and spines expressing tdTomato at four different regions across the natural focal plane as indicated by the colour of the border. Despite some reduction in optical resolution towards the edges of the imaging volume, spines can still be resolved.

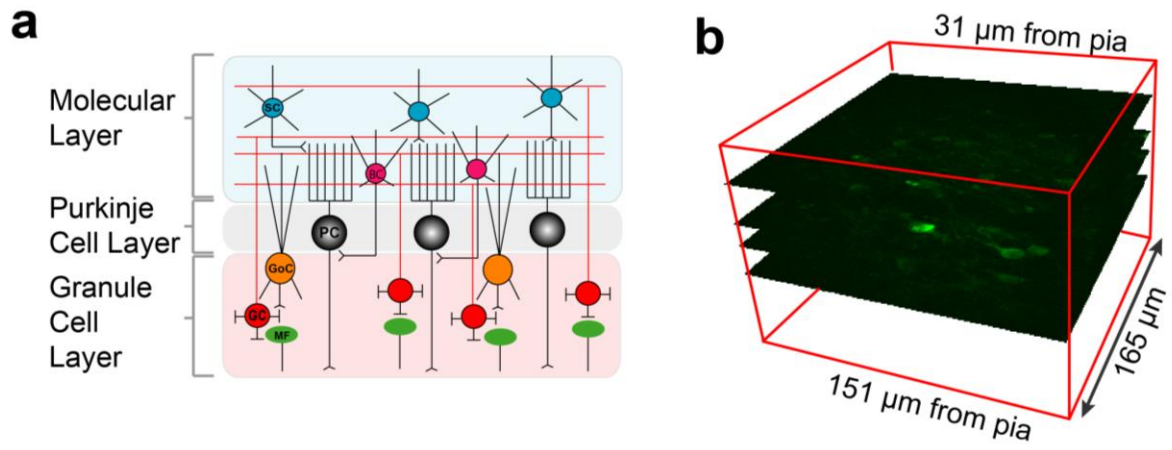

Supplementary Figure 5

Imaging across layers of the cerebellar cortex of an awake mouse.

a) Schematic diagram showing basket, stellate, Golgi, granule and Purkinje cells, (BC, SC, GoC, GC, and PC, respectively) together with mossy fibres (MF) and their location within the three-layered structure of the cerebellar cortex. **b**) AOL Z-stack of a mouse expressing GCaMP6f in the cerebellum, showing the position of the four 256 x 256 voxel planes that were imaged.

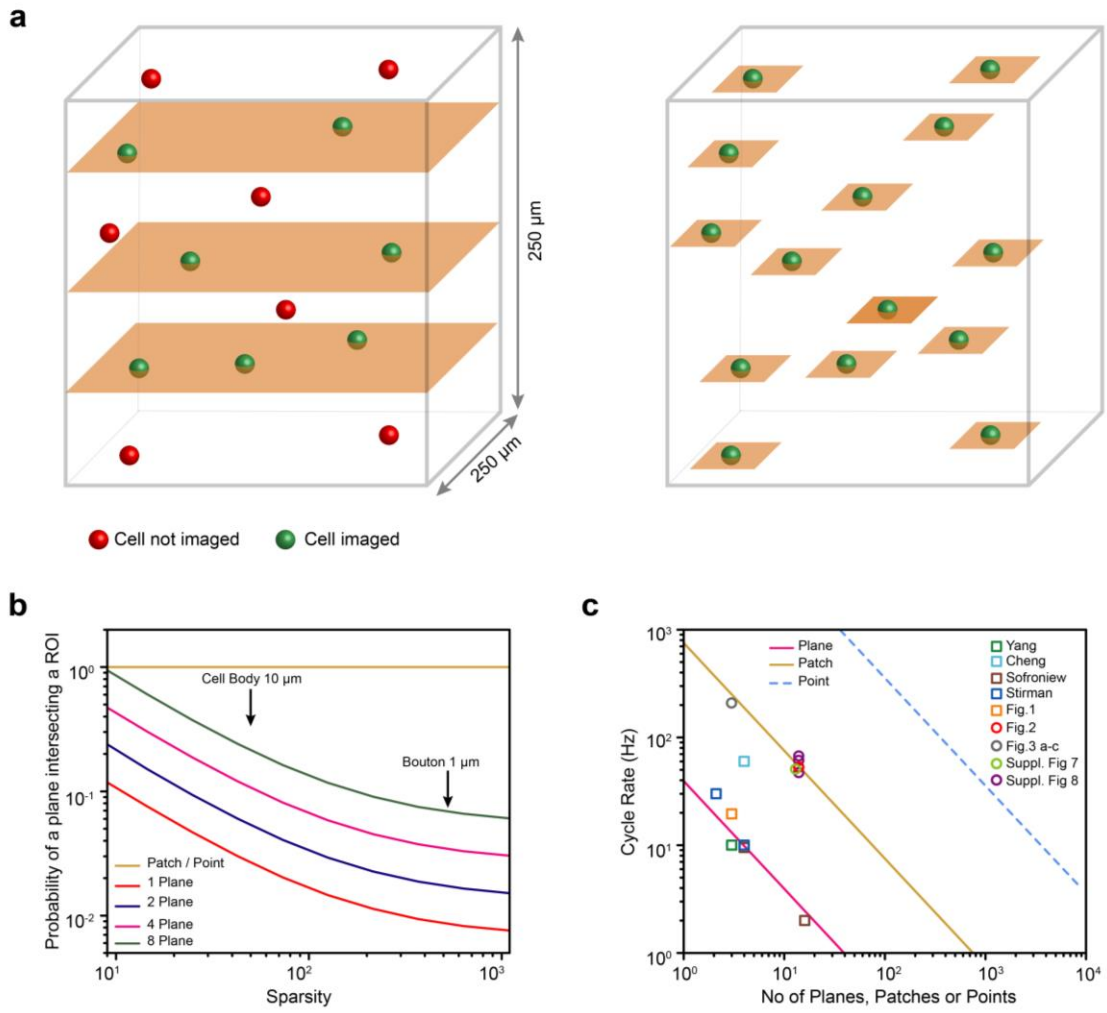

Supplementary Figure 6

Comparison of multi-plane imaging and user selected random access patch imaging for monitoring sparsely distributed cells.

a) Schematic diagram of 250 µm x 250 µm x 250 µm imaging volume with 14 neuronal cell bodies randomly distributed at low density. Left: cell bodies intersected (green) by three imaging planes (orange shading), cell bodies not intersected (red) by imaging planes. Right: user-selected patches (orange shading) aligned to intersect each cell body (green), giving probability of intersection is 100%. **b**) Probability of intersecting randomly positioned neuronal compartments as function of their sparsity (defined as Z dimension of the imaging volume/Z dimension of structure of interest) with multi-plane imaging and patch/point imaging. Arrows indicate the sparsity of two common structures of interest assuming 14 fall within the imaging volume. **c**) Estimated cycle rate for plane (magenta line, 50 ns dwell time with 512 x 512 voxels), patch (yellow line, 50 ns dwell time with 51 x 50 voxels), and point imaging (blue dashed line, 4 µs dwell time) as function of number of planes, patches and points imaged. Examples of multi-plane imaging (squares) and patch imaging (circles). Liquid crystal spatial light modulator multi-plane (green square, Yang et al. Ref 16). Space time multiplexed multi-plane imaging (light blue square, Cheng et al. Ref 17). Multi-plane imaging with large field of view two photon mesoscope (brown square, Sofroniew et al. Ref 23). Multi-plane imaging with expanded field of view two photon microscope (dark blue square, Stirman et al. Ref 24). Multi-plane imaging with AOL (orange square, Fig. 1). AOL patch imaging speed is shown in circles, Fig. 2 (red), Fig. 3a-c (grey), Suppl. Fig. 7 (green) and Suppl. Fig. 8 (purple, note that one of the four circles is behind the red).

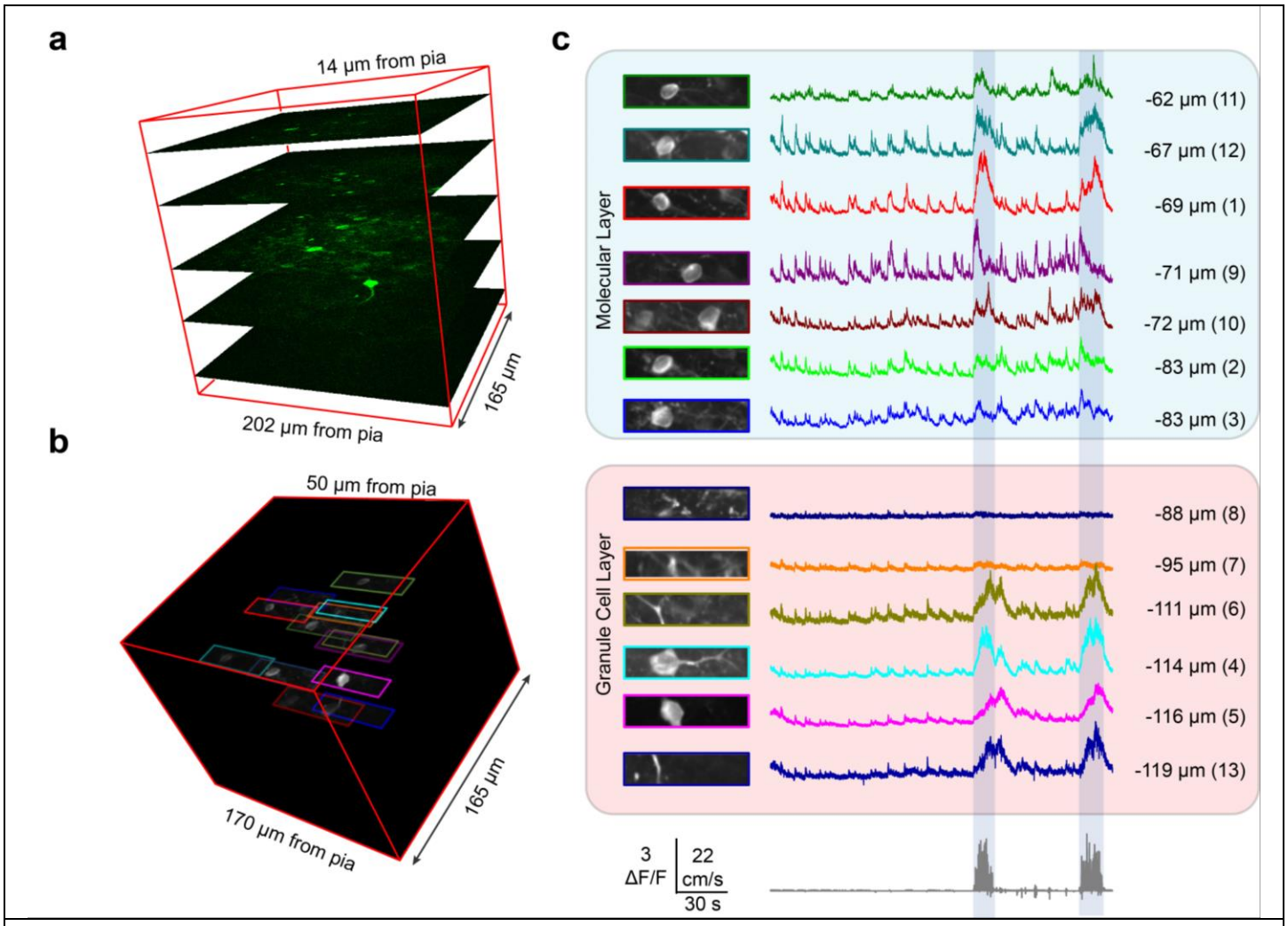

Supplementary Figure 7

Random-access patch imaging across layers in the cerebellum of an awake behaving mouse with *post hoc* movement correction.

a) AOL Z-stack of molecular and granule cell layers in the cerebellum of a mouse expressing the Ca2+ indicator GCaMP6f. **b**) Location of 13 X-Y patches (171 x 46 voxels, 73.5 µm x 19.8 µm) within the imaging volume in panel a, distributed between 62 µm to 119 µm below the pia (see Supplementary Video 4 for patch fluorescence during part of recording). **c**) Averaged images of cellular structures scanned near-simultaneously at 50 ns/voxel in the 13 patches after *post hoc* correction for brain movement. Traces to the right show ΔF/F responses extracted from each patch with a 50.6 Hz sampling rate for a complete 13 patch cycle. Grey trace at the bottom shows the speed of locomotion of the animal on the cylindrical wheel. Grey shading indicates periods of locomotion. Vertical bar indicates normalised change in fluorescence (ΔF/F) together with speed of locomotion (cm/s) and horizontal scale bar indicates time (s).

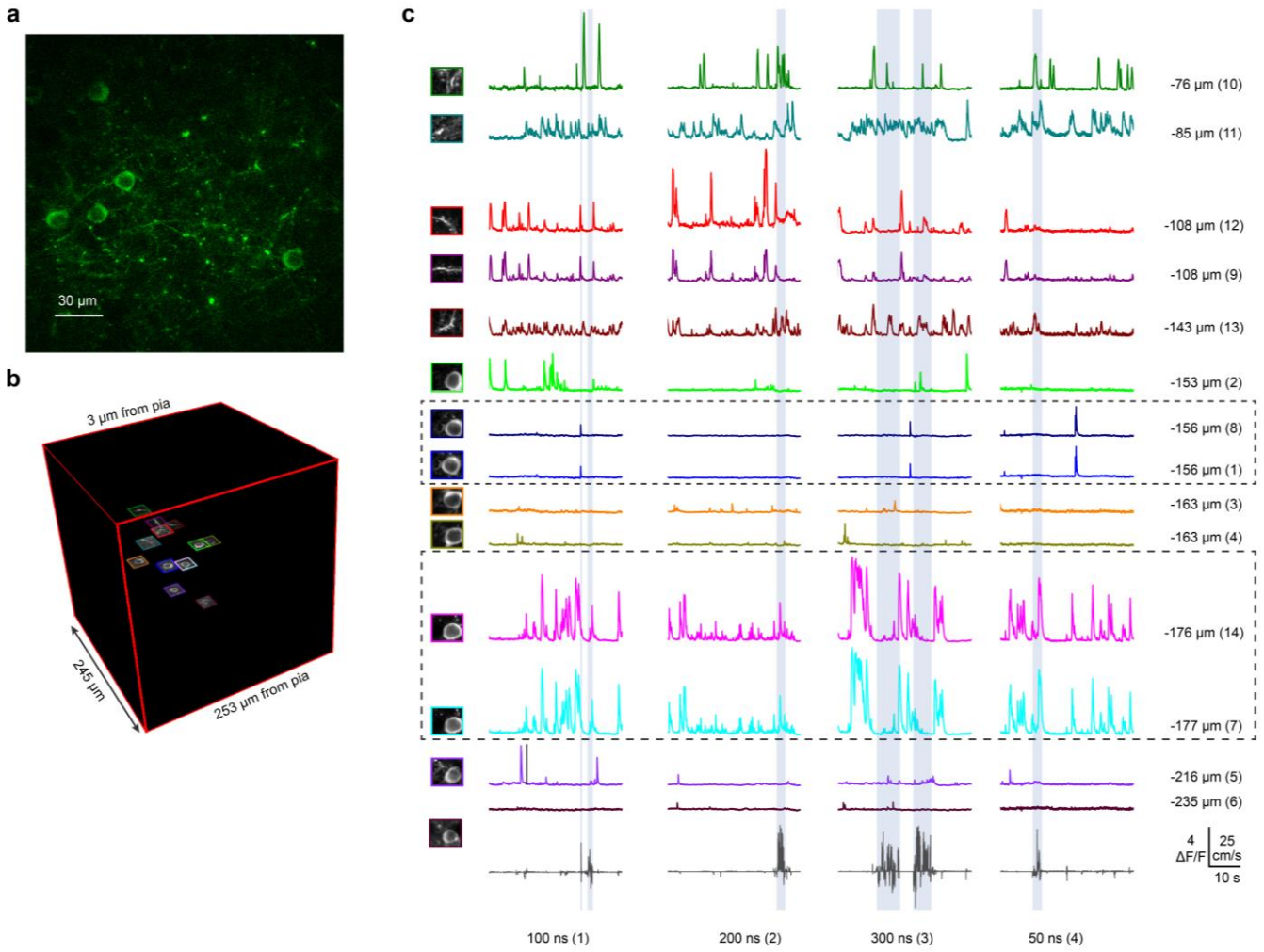

Supplementary Figure 8

Random-access patch imaging of layer 2/3 neurons expressing only GCaMP6f in primary visual cortex of an awake behaving mouse using different dwell times and post hoc movement correction.

a) Image from a Z-stack showing cells in layer 2/3 visual cortex sparsely expressing GCaMP6f. **b**) Location of 14 selected X-Y patches (46 x 40 voxels, 22 µm x 19.4 µm) within the imaging volume, distributed between 76 µm to 235 µm below the pia. **c**) Averaged movement corrected images of cellular structures scanned near-simultaneously in the 14 patches. Traces to the right show ΔF/F responses extracted from each patch when imaged at 50, 100, 200 and 300 ns/voxel dwell time, which gave sampling rates of 67 Hz, 61 Hz, 53 Hz, 47 Hz for the complete 14 patch cycle. Numbers within brackets at bottom indicate measurement sequence. Recordings were filtered using a 5-point running average and arranged in order of data acquisition. Depth and patch numbers are indicated on the right. Dashed boxes indicate instances where two patches monitored the same soma. Grey trace at the bottom shows the speed of locomotion of the animal on the cylindrical wheel. Grey shading indicates periods of locomotion. Vertical bar indicates normalised change in fluorescence (ΔF/F) together with speed of locomotion (cm/s) and horizontal scale bar indicates time (s).

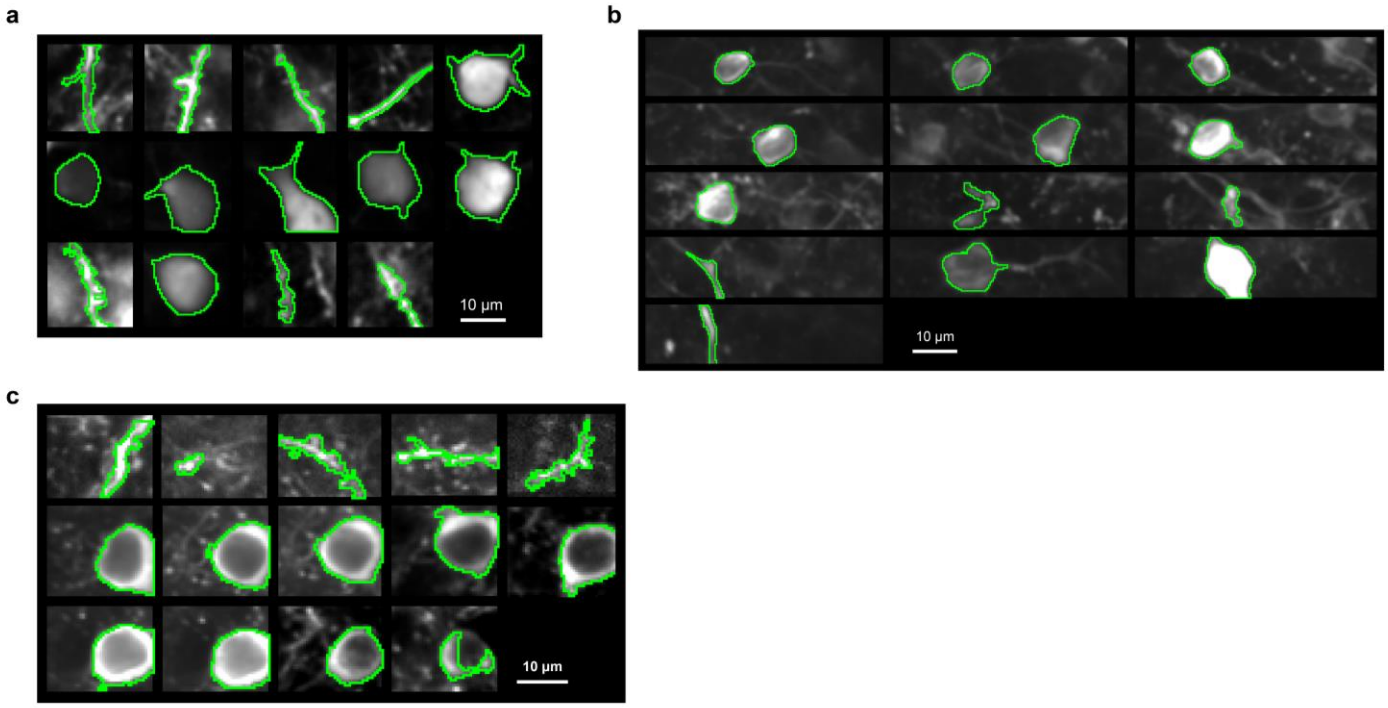

Supplementary Figure 9

Masks used to extract functional data.

a) Patch images following *post hoc* movement correction from Figure 2 together with the regions (masks) from which the fluorescence intensity data was extracted from the image time series (area within green contour lines). **b**) as for (**a**) but for data in Supplementary Fig. 7. **c**) as for (**a**) but for Supplementary Fig. 8.

Supplementary Table 1. Performance comparison of line-scan speeds and other key parameters of two-photon scanning microscopes reported in the literature.

Scanning Device	Min. Dwell Time (µs)	Max. line-scan rate at		Arbitrary 3D jump time	Z scanning	3D Pointing	Random Access Imaging of ROIs	Reference
		z=0 # (kHz)	z≠0 # (kHz)					
2st generation compact AOLM	0.05	20	20	24.5 µs	N	Y	Y	Present Work
1st generation compact AOLM	1	1.86	-	24.5 µs	N	Y	N	Kirkby and Fernandez-Alfonso (Refs.6, 8)
AOLM	1.65	~ 1	~1**	10-20 µs	N	Y	N	Katona (Ref. 9)
LOTOS	0.05	100	-	-	N	N	N	Chen (Ref.12)
Ultrasound Lens	0.025	1*	910	-	Y	N	N	Kong (Ref. 3)
Galvo + Piezo	-	1*	1	100 ms***	Y	N	N	Gobel (Ref. S1)
Resonant Galvo	0.06	24 or 32	24 or 32	-	N	N	N	Cheng (Ref.20)
Piston Mirror	0.72	1*	2.7	1 ms***	Y	N	N	Botcherby (Ref. 4)
Galvo + Electrical Tunable Lens	-	1*	1	30 ms***	Y	N	N	Grewe (Ref.2)
Galvo + SLM	-	1*	1*	3ms	N	N	N	Yang(ref 16)
Mesoscope	0.04	24	24	6ms	N	N	Y	Sofroniew (Ref S2)
Multi region wide field	0.25	7.6	7.6	-	N	N	N	Stirman (Ref S3)

Values are adjusted for 512 voxel line-scan from reported numbers.
*Standard Galvanometer mirror scan speed.
** Partial line-scan.
*** Estimated from quoted bandwidth

Supplementary Note 1. Acousto-Optic Lens (AOL) operation, duty cycle and line-scanning. Spherical AOLs consist of two pairs of AODs that are arranged orthogonally. For each AOD pair the acoustic waves travel in opposite directions. The AOL focus is determined by the slope (chirp) of the acoustic frequency drive as a function of time and the lateral deflection is set by the fixed frequency offset between the drive waveforms being fed into each of the two pairs of AODs that makeup the AOL. Previous AOL designs have not been able to perform full-frame line-scans out of the natural focal plane of the objective, and have instead used pointing mode (or short line-scans). In pointing mode, 'lines' can be created from voxel-by-voxel series of focal points and XY images can be built up of such lines. But using pointing mode for full frame imaging is slow because the duty cycle is dominated by the AOD fill time (24.5 μs), when no photons are being collected. This is because altering the position of the focused laser beam, from one voxel to the next, requires that the AOD apertures are refilled by a new acoustic wave with different properties. Since this is considerably longer than the dwell time (typically 1 – 4 μs) the duty cycle is low (**Supplementary Fig. 1a**) and image formation is slow. By contrast, our second generation AOL design, reported here, can perform fast, continuous full-frame line-scans of a focussed laser beam at any focal plane within the imaging volume. The line-scan rate is determined by two factors in our system: the time it takes to scan each line (dwell time x number of pixels) plus the time it takes to refill the crystals to reposition the beam before the next line is acquired (24.5 μs). Since line-scans consisting of up to 1024 voxels can be generated during a single AOL fill time, this mode of imaging has a much higher duty cycle, despite the short dwell times (**Supplementary Fig. 1a)** and full frame imaging is fast.

Supplementary Note 2. Full-frame line-scanning with an AOL and the trade-off between dwell time and imaging volume for full-frame line-scans. A line-scan can be performed by an AOL by varying the frequency offset of the AOD pair as a function of time. At the natural focal plane all of the acoustic drive frequency bandwidth over which diffraction occurs efficiently (i.e. 30-50 MHz) can be used for the time varying offsets required for lateral scanning[6]. However, when continuous

line-scans are performed above or below the natural focal plane, the drive frequency bandwidth of the AODs has to be shared between the ramped frequency drive required for focussing to a particular plane and the time varying offsets required to scan laterally. As the amount of AOL focus increases, the slope of the acoustic drive increases and the time before the drive frequency exceeds the AOD bandwidth and enters low diffraction efficiency regions, decreases. Thus there is less time available for performing a line-scan as the AOL focus increases. To overcome this trade-off, we increased the line-scan speed by reducing the voxel dwell time from 1-4 μs in the first generation system to 50-500 ns in the second generation system. With the improved on-axis AOD crystal design, which improved transmission and increased the scan angle of the AOL, we can perform full frame line-scan imaging over a volume of 250 x 250 x 250 μm at 50 ns dwell time. The shorter line-scans used for ROI patch imaging take proportionately less bandwidth and can therefore be imaged using longer dwell times if necessary (50–500 ns**; Supplementary Fig. 2c,d; Supplementary Fig. 8**).

Supplementary Note 3. Comparison of 3D two-photon imaging methods

The specifications summarised in Supplementary Table 1 and Supplementary Figure 6, only provide part of the information required to choose the most appropriate 3D imaging system for a particular application, because several other factors contribute to the maximum practical 3D imaging rate during functional imaging (see ref S4 for excellent in-depth review of 3D imaging technologies). These include the dwell time per ROI and rate of dye bleaching, which both affect the SNR. These factors are difficult to relate to the properties of mechanical scanning technology (e.g. repositioning speed in 3D, line scan rate and duty cycle) as they depend on the spatial distribution of ROIs in 3D space and the fluorophore. Moreover, although it is known that that high scan speed reduces cellular damage[12], the optimal values for line scan rate are likely to be indicator-specific because brightness and bleaching rates vary widely across the fluorescent probes used. Nevertheless, the high speed 3D random access scanning functionality of our AOL microscope, which enables ROIs to be imaged selectively wherever they are located in the imaging volume,

together with variable dwell times, provides the flexibility to image efficiently irrespective of the spatial distribution of the ROIs.

References

S1 Gobel, W., Kampa, B. M. & Helmchen, F. Imaging cellular network dynamics in three dimensions using fast 3D laser scanning. *Nat Methods* **4**, 73-79, doi:10.1038/nmeth989 (2007).

S2 Sofroniew, N. J., Flickinger, D., King, J. & Svoboda, K. A large field of view two-photon mesoscope with subcellular resolution for in vivo imaging. *eLife* **5,** e14472 (2016).

S3 Stirman, J.N., Smith, I.T., Kudenov, M.W., Smith, S.L. Wide field-of-view, multi-region, two-photon imaging of neuronal activity in the mammalian brain. *Nat Biotechnol*. **34**, 857-62. doi: 10.1038/nbt.3594 (2016).

S4 Ji, N., Freeman, J. & Smith, S.L. Technologies for imaging neural activity in large volumes. *Nat Neurosci.* **19**, 1154-64. doi: 10.1038/nn.4358 (2016).